Plant patch hydrodynamics in streams: Mean flow, turbulence, and drag forces

Fabio Siniscalchi,[1] Vladimir I. Nikora,[1] and Jochen Aberle[2]

Received 16 June 2011; revised 17 November 2011; accepted 22 November 2011; published 19 January 2012.

[1] This paper investigates the effects of a finite-size vegetation patch on flow turbulence, variations in drag forces experienced by individual plants within the patch, and flow-drag interrelations. The experiments were conducted in a 32 m long laboratory flume with a 2.8 m long artificial patch. The plants were arranged to form a staggered pattern and three flow scenarios were tested. Velocities were recorded with an acoustic doppler velocimeter, whereas specifically designed devices were used to simultaneously measure the drag forces acting on nine plants within the patch. For all studied cases, the results show zones of increased turbulent energy close to the leading edge and along the patch canopy top, where turbulence shear production is enhanced. Zones of negative Reynolds stresses $-\overline{u'w'}$ are found inside the patch and they reflect the influence of plant morphology, which affects the shape of the longitudinal velocity profile and associated turbulent fluxes. Modifications to the power spectral densities of velocity by the plants indicate the emergence of two plant-induced mechanisms of energy production, which are most likely related to the wake turbulence and shear layer turbulence. Drag fluctuations appear to be correlated with the velocity field, with this correlation being especially profound at the highest-studied flow rate. The data suggest that the highlighted correlation stems from flow-plant interactions at the top of the vegetation canopy, likely due to the presence of large three-dimensional coherent structures.

Citation: Siniscalchi, F., V. I. Nikora, and J. Aberle (2012), Plant patch hydrodynamics in streams: Mean flow, turbulence, and drag forces, *Water Resour. Res.*, *48*, W01513, doi:10.1029/2011WR011050.

1. Introduction

[2] Understanding the physical processes associated with the presence of aquatic vegetation in open-channel flows is vital in order to assess vegetation-induced modifications of flow resistance, sediment transport and river morphology. The additional drag generated by plants leads to velocity reduction within the vegetation canopies and to an increase in water depth [*Nepf*, 1999], enhancing flooding risks. Regions of decreased bed shear stress, often observed in vegetated channels [e.g., *Maltese et al.*, 2007; *Sukhodolov and Sukhodolova*, 2010], may significantly enhance sedimentation and retention of particles [*Nepf and Ghisalberti*, 2008] affecting channel morphodynamics and water quality.

[3] In general, vegetation patches cannot be considered as conventional obstructions to the flow (e.g., weirs or piers) since they are porous and formed by flexible plants, which may or may not interact with each other. Plant survival within a patch is highly dependent on their capability of withstanding drag forces [e.g., *Koch et al.*, 2006] by adopting various mechanisms such as static or dynamic reconfiguration [e.g., *Sand-Jensen*, 2003; *Nikora*, 2010]. It is likely that the plant location within the patch is an important factor since the magnitude of the drag forces may depend on local mean velocities and turbulence characteristics [*Nikora*, 2010]. However, variations of instantaneous and time-averaged drag forces and their control by the flow within aquatic patches have not been systematically studied yet and remain largely unknown.

[4] The individual plants within submerged patches exhibit a wide range of morphologies and are generally flexible. The responses of aquatic plants to drag forces imposed by the flow depend on the combined effects of these features that may vary significantly within a patch. This complexity of plant shapes and mechanical properties is reflected in an intricacy of flow-plant interactions and cannot be properly simulated with rigid cylinders employed in many studies. Flexible surrogate plants have been used by a number of authors [e.g., *Nepf and Vivoni*, 2000; *Folkard*, 2005; *Ghisalberti and Nepf*, 2006; *Maltese at al.*, 2007; *Luhar and Nepf*, 2011], who highlighted desires for more comprehensive studies and who identified potential directions for next steps.

[5] Another important aspect of flow-plant interactions, awaiting clarification, relates to the potentially significant effect of a patch size. The flow encountering and entering the patch needs a transition length to reach a new equilibrium condition [e.g., *Ghisalberti and Nepf*, 2009]. Most studies to date have extensively analyzed the part of canopies where flow is fully developed and reached this equilibrium condition, both experimentally [e.g., *Nepf and Vivoni*, 2000; *Järvelä*, 2005; *Ghisalberti and Nepf*, 2006; *Lefebvre et al.*, 2010; *Folkard*, 2011b] and numerically [e.g., *Choi*

[1]School of Engineering, University of Aberdeen, Scotland, UK.
[2]Leichtweiß-Institute for Hydraulic Engineering and Water Resources, Technische Universität Braunschweig, Braunschweig, Germany.

0043-1397/12/2011WR011050

Table 1. Experimental Matrix

Scenario	Flow Rate Q ($m^3 s^{-1}$)	Bed Slope S_0 (%)	Water Depth H[a] (cm)	Section-Averaged Velocity U_s ($m s^{-1}$)	$Re = \frac{U_S H}{\nu} = \frac{Q/W^b}{\nu}$	$Fr = \frac{U_S}{\sqrt{gH}}$
High	0.120	0.23	28.3–30.6	0.65–0.71	200,000	0.38–0.42
Medium	0.081	0.10	28.6–30.0	0.45–0.47	135,000	0.26–0.28
Low	0.036	0.05	29.5–30.0	0.20	60,000	0.12

[a]The water depth was not constant along the flume because of the presence of the patch: It varied within the ranges shown. As a consequence, section-averaged velocity and Froude number also varied.
[b]W denotes the flume width (equal to 0.60 m).

and Kang, 2004; *Poggi et al.*, 2004]. Few studies, however, have examined the transition regions, i.e., the entrance and exit regions of a vegetation patch, where the effects of flow gradients and heterogeneities may prevail [e.g., *Sukhodolov and Sukhodolova*, 2006; *Bouma et al.*, 2007; *Neumeier*, 2007; *Folkard*, 2011a; *Zong and Nepf*, 2010; *Souliotis and Prinos*, 2011]. Such hydrodynamic zones are likely to be predominant in patches of finite length, which are widespread in natural rivers.

[6] To address the highlighted knowledge gaps, the present study explores the interactions between a turbulent open-channel flow and a finite-size patch constructed of artificial flexible plants. In particular, the objectives of the paper are: to identify and quantify the flow structure around and within a submerged vegetation patch, to explore coupling between turbulent characteristics of flow and drag forces acting on the plants and their variability within the patch, and to propose a conceptual model of patch hydrodynamics that would explain the observations.

2. Methodology

[7] The experiments were conducted in a 32 m long, 0.6 m wide, and 0.4 m deep tilting flume in the hydraulic laboratory of the Leichtweiß-Institute for Hydraulic Engineering and Water Resources, Technische Universität Braunschweig, Germany. The water level was controlled through a weir located 25 m from the flume entrance and the bed roughness was formed by a rubber mat with uniform pyramidal shaped elements 3 mm high. From a combination of flow discharges, bed slopes, and weir positions, three flow scenarios were selected and tested (i.e., low (L), medium (M) and high (H), Table 1).

[8] A 2.8 m long vegetation patch was prepared by fixing 53 artificial flexible plants on the flume bed in a staggered pattern, with a spacing of 20 cm between them (Figures 1 and 2). The artificial plants used in the experiments are described in detail by *Schoneboom and Aberle* [2009] and *Schoneboom et al.* [2010]. First, artificial plants were chosen to ensure that plant properties did not change over the 3 weeks taken to complete the experiments. Second, flexibility and morphological complexity of the selected artificial plants resemble riparian vegetation, e.g., young poplars growing on floodplains, as evidenced by tests conducted with a branch of real poplar growing next to the Oker river, in Braunschweig [*Schoneboom et al.*, 2008].

[9] Some plants in the patch had to be placed close to the sidewalls (Figure 1), and therefore six of the 12 leaves were removed from these plants to maintain a constant plant density (Figure 2b), similar to the study of *Schoneboom et al.* [2010]. Because of the presence of the patch, the water depth was not uniform along the channel, and it was measured with 11 piezometers installed between 6 and 20 m from the flume entrance. For all experiments, the aspect ratio (W/H, W is the flume width, H is the water depth) ranged from 1.96 to 2.12, and the relative submergence (H/h_{veg}, h_{veg} is the height of the bent patch) ranged from 1.2 to 1.5. These parameters are comparable to those considered by other authors, e.g., *Nepf and Vivoni* [2000] and *Ciraolo et al.* [2006]. The small aspect ratio ($\sim$2) indicates the presence of secondary currents, most likely occupying the whole cross section. For our study, however, their effect should not be influential due to the dominance of flow-patch interaction effects. As for the relative submergence, their values are typical for vegetated streams [e.g., *Sand-Jensen and Pedersen*, 1999].

[10] Velocity measurements were made with a Nortek 10 MHz acoustic doppler velocimeter (ADV), which has an accuracy of 1% of measured velocity (available at http://www.nortekusa.com). The sampling frequency was set to 50 Hz and the data handling followed *Goring and Nikora* [2002]. The coordinate system is represented by x for streamwise, y for lateral, and z for vertical directions (with velocity components u, v, and w, respectively). The origin

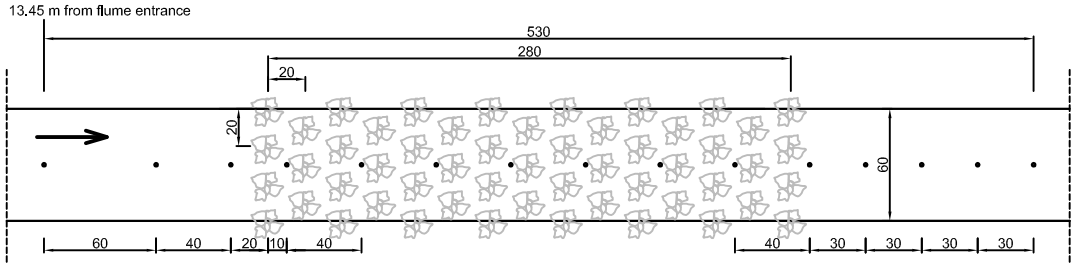

Figure 1. Plan view of the experimental setup (type A). All units are in centimeters unless otherwise indicated. Black dots indicate the positions of the velocity measurement verticals.

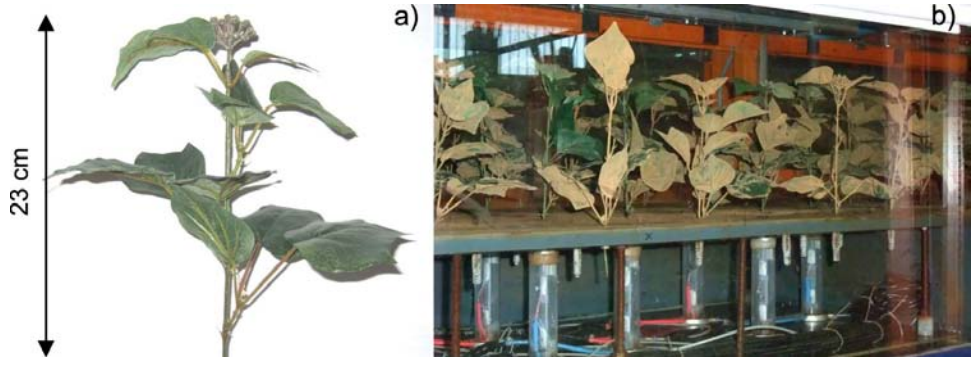

Figure 2. An example of the type of artificial plant used in the experiments (a) and the drag force test section (b); note the drag force sensors (DFSs) placed beneath the flume bed.

is fixed at the bed, at the flume centerline, 13.45 m from the flume entrance, corresponding to the position of the first measurement vertical (see below).

[11] Nine drag force measurement sensors (DFSs), described in detail by *Schoneboom et al.* [2008], were used in order to measure the drag forces exerted on the plants within the patch. Each device consisted of a vertical stainless-steel beam acting as a cantilever, with a bottom end rigidly fixed to a base plate. A single plant was fixed at the top end of the beam that is slightly protruding through a head plate (Figure 2b). The drag force exerted on the plant was measured using eight strain gages configured as two Wheatstone full bridges, positioned on the centerline of the beam. To protect the strain gages from water, a hollow plastic tube was connected to the head plate. The devices were placed beneath the flume bed, in a 1.5 m long test section located 15.1 m from the channel entrance, in such a way that they did not interfere with the flow (Figure 2b). The accuracy of these instruments was 1%–2% of the measured force [*Schoneboom et al.*, 2008]. The sampling frequency was set to 200 Hz.

[12] Two types of experiments were conducted: profile measurements (type A) and long-term measurements (type B). The aim of the first type of experiments was to obtain data to describe flow turbulence around and within the patch. Therefore, only velocity measurements were made at 15 verticals along the flume centerline (Figure 1). At each vertical, measurements were made at 15 positions through the water column, making 225 measurement points in total per flow configuration. An exception is the high-flow rate scenario, where velocities at the highest position at the downstream six verticals were not measured because of air bubbles often attached to the ADV transducers during the experiments. Each recording lasted 120 s.

[13] The aim of the type B experiments was to obtain the data for the analysis of drag force variations along the patch and their coupling to the surrounding turbulent flow. Each experiment lasted 15 min, with a simultaneous recording of the velocity and drag forces acting on nine plants (at 50 and 200 Hz, respectively). Velocities were recorded at only two points, 20 cm upstream of the patch leading edge and within the drag measurement test section. In the experiments, it was decided first to place the ADV at the upstream position and collect the synchronous data of velocity and drag forces acting on nine plants, then the ADV was placed in the second position (within the patch) and again the synchronous measurements were recorded. The two sets of drag force data were expected to be statistically equivalent, and therefore results related to the same plant were averaged when performing the data analysis. Another issue relates to the location of the plants equipped with DFSs. The test section where such devices could be placed was fixed and only 1.5 m long. Therefore, in order to evaluate the drag forces acting along the entire patch, from the leading to the trailing edge, it was decided to move a number of plants upstream or downstream of the test section, obtaining three configurations (Figure 3). In this way, measurements of the drag force acting on the individual plants in the centerline of the patch, for its entire length, were obtained. To summarize, three configurations were analyzed for each flow set-up (Table 1), and for each configuration two experiments were conducted, measuring the velocity upstream of the patch first and then inside the test section. The vertical position of the ADV sampling volume was chosen in such a way that the probe did not affect the surrounding plants. It was decided to align the tip of the probe with the top of the patch, which was different for each experimental scenario because of different bending angles. Therefore, the sampling volume was located at $z =$ 15, 17, and 19 cm, for high-, medium-, and low-flow scenarios, respectively.

[14] The analysis of the collected data first focused on the bulk statistics (statistical moments) of velocity and drag measurements. Turbulence parameters such as turbulent kinetic energy, Reynolds stresses, and eddy viscosity provided information on turbulent energy production and fluxes. Spectral analysis of velocity and drag time series was also used to determine the main frequency components of the signals. Coupling of the data was examined with cross-correlation and coherence functions.

[15] The errors involved in the estimates of the parameters used are briefly outlined below. For the flow rate Q, the accuracy of the magnetic flowmeter was fixed to 0.5% of the flow rate (instrument specifications). The error of the bed slope measurement is related to the measurement of the vertical elevation of the flume in a specific section, which was evaluated with a ruler (resolution 0.5 mm). Thus, for the lowest slope, the maximum relative error e_r was found to be 2.4%. The water levels in the piezometers were measured with Vernier depth gages (resolution 0.1 mm), and the greatest relative error of H was 0.02%. Applying the error propagation theory, e_r for the section-averaged

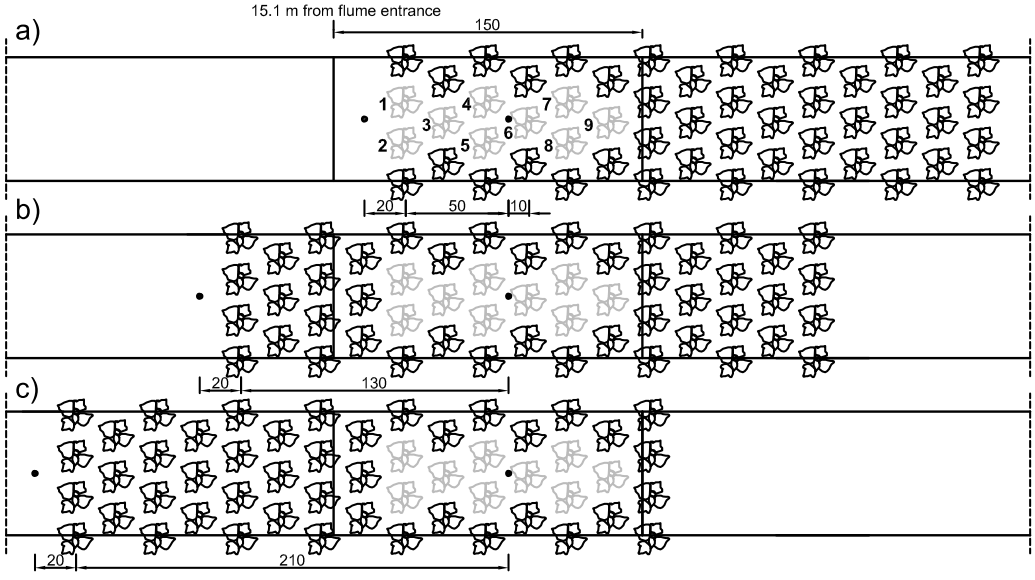

Figure 3. Configurations 1 (a), 2 (b), and 3 (c) for type B experiments. All units are in centimeters unless otherwise indicated. Gray color indicates plants connected to DFSs and black dots indicate the positions of the velocity measurements. Note that the position of the patch for type A experiments was the same as in Figure 3b.

velocity, Reynolds number, and Froude number were all estimated to be ~0.5%–2%.

[16] A quantification of the statistical errors related to the estimates of the mean and variance of velocity and drag measurements were made following *Garcia et al.* [2005]. The maximum relative standard error of $\overline{u}$ was 2.2% (low-flow scenario), with an average of 0.6%. For the variance, the maximum relative error was found to be 13.1% (low-flow scenario), with an average of 4.0%. For the drag force statistics, the maximum error on the estimate of the mean was 1.0% (high-flow scenario, plant 6, configuration 1), with an average of 0.2%. Finally, the maximum relative error for the variance was evaluated to be 15% (high-flow scenario, plant 6, configuration 1), with an average value of 3.3%.

3. Results

3.1. Flow Structure

[17] The results related to the flow structure within and around the patch are the main focus of this section, with particular attention given to background hydraulic properties, bulk turbulence parameters, and spectral description.

3.1.1. Background Hydraulic Properties

[18] The presence of a finite patch modifies channel resistance and conveyance, at least locally, and leads to deviation from uniform flow conditions. Figure 4 shows the water depth measured between 6 and 20 m from the flume entrance for the three studied flow conditions (H, M, and L, Table 1). In all cases, the water level tends to increase in front of the patch and reaches a maximum at the leading edge. After this point, the water surface elevations decrease and their minimum is observed at the patch exit. Further downstream, the water depth tends to return to the initial undisturbed upstream value. The difference in water levels between upstream and downstream patch edges, ΔH, grows as flow rate increases. Indeed, at the low-flow rate (L) $\Delta H = 5$ mm, whereas at the highest-flow rate (H) it reaches 23 mm (Table 1). Similarly, the longitudinal gradients of the section-averaged velocity varied with increasing flow

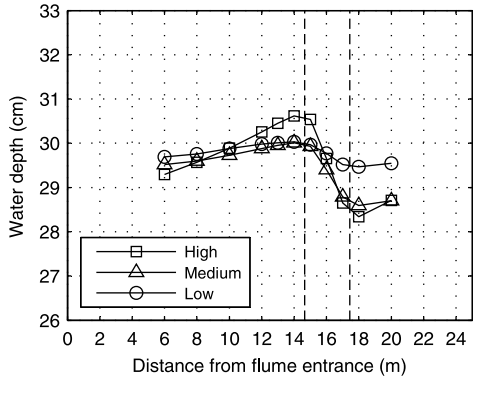

Figure 4. Water depth profiles along the flume. Dashed lines indicate leading and trailing edges of the patch.

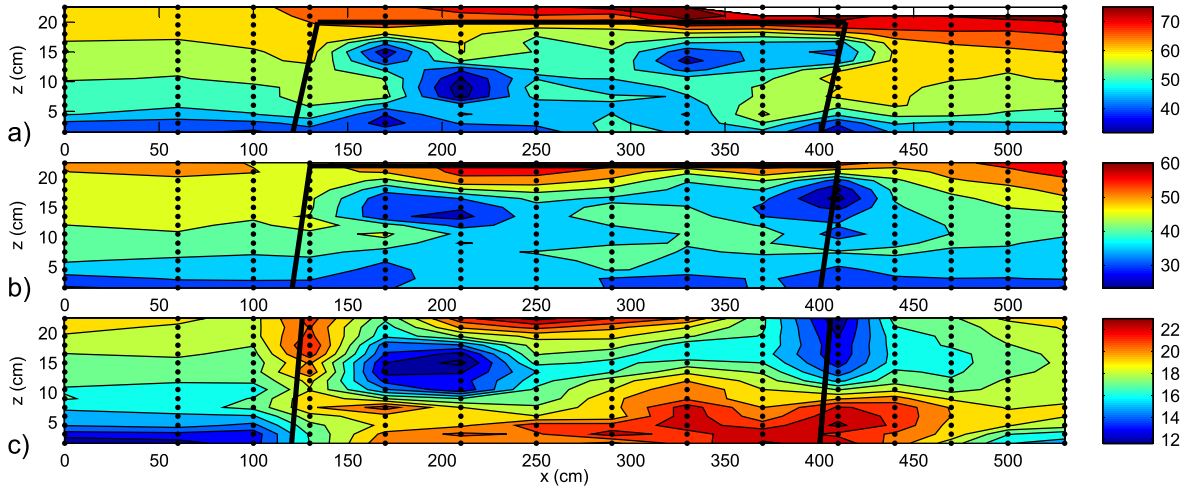

Figure 5. Contour lines of mean longitudinal velocity (cm s^{-1}) for (a) high-, (b) medium-, (c) and low-flow rates. Note the different scales for the color legend. Black dots indicate the measurement positions; the thick lines show the area occupied by the patch. The upper boundary of the patch (horizontal line) was visually evaluated by placing a vertical ruler in the vegetated zone. These measurements were not expected to be precise, but they provided adequate estimates of the patch height.

rate from -0.0004 s^{-1} to -0.0043 s^{-1} in front of the patch and from 0.0017 s^{-1} to 0.0236 s^{-1} within the patch.

3.1.2. Bulk Turbulence Parameters

[19] The contour lines of the time-averaged longitudinal velocity $\overline{u}$ at the flume centerline are shown in Figure 5 for all scenarios. The flow encountering the patch can be divided into two regions. Inside the patch, the velocity is strongly reduced, whereas above it the flow is highly accelerating. At the trailing edge such a division starts to disappear, and the individual velocity profiles show a tendency to return to the undisturbed upstream condition, which would be expected further downstream from the measured region. It is interesting to note that for the low-flow scenario, however, a zone of increased velocity is also found near the bed and it extends all along the patch.

[20] The turbulent kinetic energy (TKE) of the flow, evaluated as $0.5(\overline{u'^2} + \overline{v'^2} + \overline{w'^2})$, represents the mean energy per unit mass associated with turbulent eddies. For all cases, we notice two main regions of increased TKE inside the patch. The first zone is located close to the leading edge, and the second one is generated at the top of the patch. Figure 6 shows the contour lines of TKE for the high-flow rate scenario, which are similar to the medium- and low-flow rates.

[21] Reynolds stresses $-\overline{u'w'}$ were also evaluated and a typical example of their spatial distribution is plotted in Figure 7. As for the TKE, one can note zones of high stress close to the top of the vegetation. Inside the patch, however, zones of negative Reynolds stresses appear which were not expected. Such zones are mainly found in the lower part of the patch, and they are likely a result of the turbulence generated by dynamically reconfiguring leaves, which affect the vertical velocity profile and the transport of momentum.

[22] In order to better visualize the modifications of $\overline{u}$, TKE, and Reynolds stress by the patch, Figure 8 presents selected vertical profiles (i.e., at $x = 0$, 290, and 530 cm) of these parameters for high- and low-flow rates. It should be noted that the flow is already affected by nonuniformity at $x = 0$ cm (i.e., 1.2 m upstream of the leading edge of the patch, see Figure 4), and therefore vertical profiles of the turbulent parameters can deviate from the standard profiles (e.g., Figure 8d or 8f).

[23] High-order moments provide further information regarding the statistical structure of velocity fluctuations. Figure 9 shows contour lines of velocity skewness $S_i = \overline{u_i'^3}/(\overline{u_i'^2})^{\frac{3}{2}}$ related to u and w components for the high-flow rate scenario. A zone of positive S_u is clearly observed downstream from the patch, in the wake, whereas S_w in the same region is negative. A similar trend is found near the top of the patch, but with opposite signs (i.e., $S_u < 0$ and $S_w > 0$). Similar results are obtained for the medium- and low-flow rate scenarios.

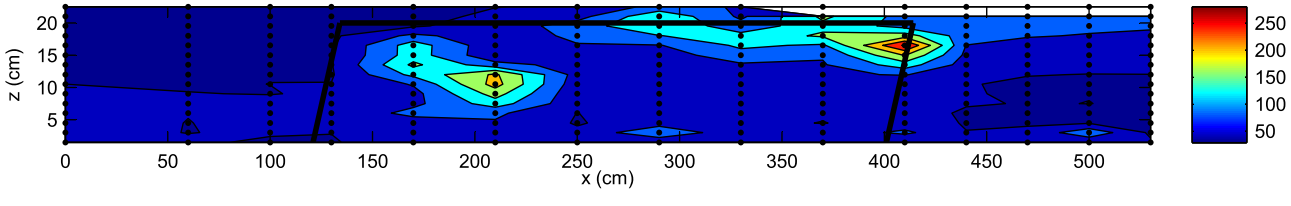

Figure 6. An example of the spatial distribution of the TKE (cm^2 s^{-2}, high-flow rate).

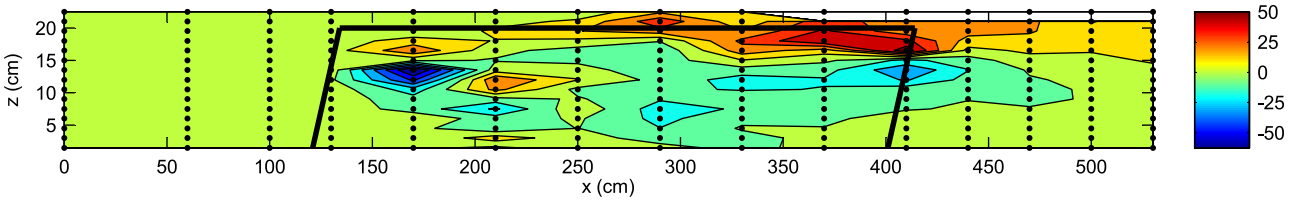

Figure 7. An example of the spatial distribution of the Reynolds stresses ($cm^2\ s^{-2}$, high-flow rate).

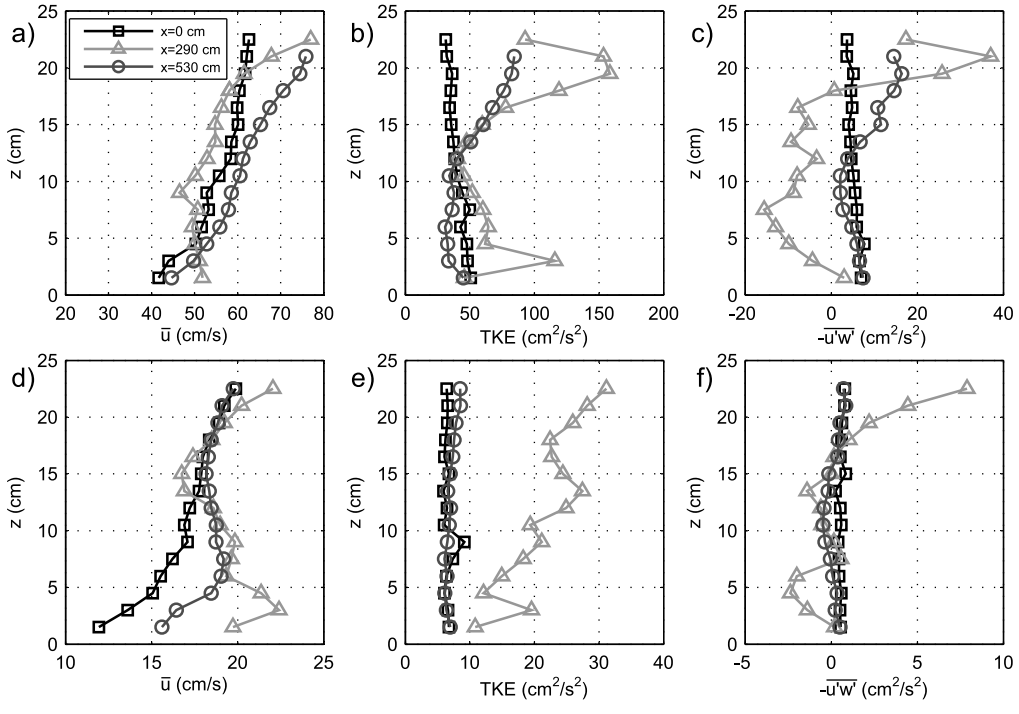

Figure 8. Vertical profiles of mean longitudinal velocity, TKE, and Reynolds stresses for high- (a, b, c) and low- (d, e, f) flow rates. In each graph three profiles are shown, evaluated at $x = 0$, 290, and 530 cm.

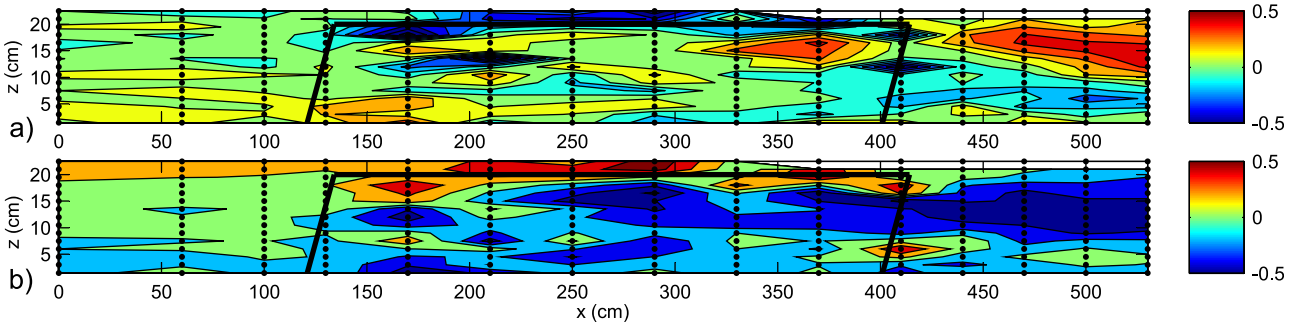

Figure 9. An example of the spatial distribution of the skewness for (a) longitudinal and (b) vertical components of velocity (high-flow rate).

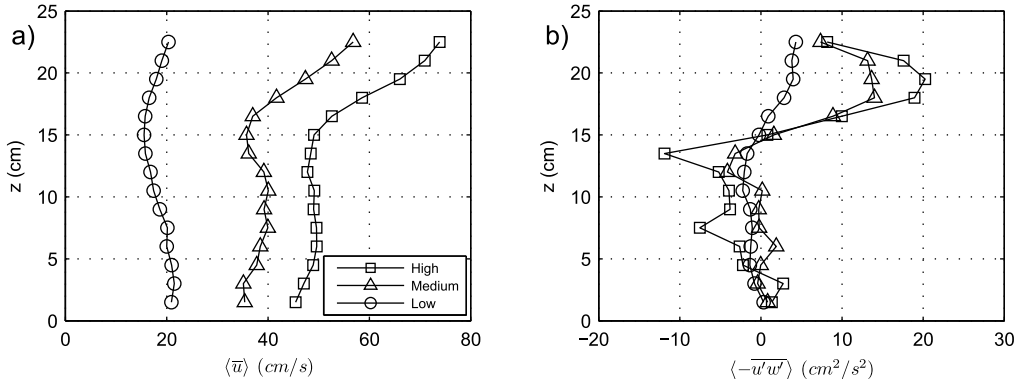

Figure 10. (a) Patch-averaged longitudinal velocity and (b) patch-averaged Reynolds stress.

[24] Figures 5–9 highlight the high level of the flow heterogeneity within and around the patch expressed in terms of the time-averaged velocity components, turbulent energy, Reynolds stresses, and skewness coefficients. In addition to this detailed description, spatial averages of these quantities can be useful for comparing the studied flow scenarios. Representative spatially averaged profiles have been obtained by averaging the time-averaged parameters along the same elevation z, considering five verticals (from $x = 170$ to $x = 370$ cm). Such spatially averaged parameters are hereafter referred to as patch-averaged and denoted with $\langle - \rangle$; the results are summarized in Figure 10. Deviations from the standard logarithmic profile of the longitudinal velocity are evident, with the flow being slower within the patch than above it, and with inflection points being clearly identifiable within the patch and at its upper boundary. In the low-flow rate scenario, however, we observe faster flow near the bed as well. Furthermore, the spatially averaged Reynolds stresses $\langle -\overline{u'w'} \rangle$ clearly show high-positive values close to the top of the patch and some negative values inside it.

[25] An estimate of the "patch-averaged" eddy viscosity ν_t within the vegetation was also obtained, as

$$\nu_t = \frac{\langle -\overline{u'w'} \rangle}{\partial \langle \overline{u} \rangle / \partial z}. \tag{1}$$

This parameter can be useful for numerical simulations involving vegetation modeling and therefore it is instructive to check its distribution, at least qualitatively. Eddy viscosity ν_t was evaluated upstream of the patch as well (considering two upstream verticals at $x = 0$ and 60 cm), and the results are shown in Figure 11. A few points have been removed from the plot because they likely reflect enhanced errors from velocity derivative estimates. Upstream of the vegetation patch, the eddy viscosity, as expected, tends to zero close to the bed, increases along the water column, and then it is assumed to approach zero again at the water surface, although the ADV could not resolve the upper part of the flow. Within the vegetation zone, no significant differences for ν_t are found among the flow scenarios. Furthermore, the parameter ν_t in most cases is positive, suggesting that the energy flux continues to be from the mean flow to turbulence (i.e., the negative sign of Reynolds stresses in some regions are balanced by the sign of the velocity derivative in the same regions).

3.1.3. Spectral Parameters

[26] Figure 12 shows the power spectral densities (PSD) of the v-component obtained from the long-term measurements (15 min) for all flow rate scenarios. The spectra present the measurements within the patch at 50, 130, and 210 cm from the leading edge of the patch (Figure 3). The transverse velocity component is selected for illustration as it highlights the high level of flow three-dimensionality and potential significance of the multiscale wake regions behind the plants and their elements. An energy input in the range of high frequencies (~5–6 Hz) is clearly observable close to the leading edge in the medium- and high-flow rate scenarios, whereas at the low-flow rate this local maximum is not easily discernible. Further downstream inside the patch, the spectral energy increases at lower frequencies as well, with a significant maximum in PSD noted in the range 1–2 Hz (medium- and high-flow rates) and 0.4–0.6 Hz (low-flow rate). These frequency ranges appear to be comparable with the frequencies associated with the Kelvin-Helmholtz instability [*Ghisalberti and Nepf*, 2002], which can be estimated from the patch-averaged velocity profiles as $f_{KH} = 0.032(\overline{U}/\theta)$, where $\overline{U}$ is the arithmetic mean between velocities above and within the patch and θ is the momentum thickness (as defined by *Ghisalberti and*

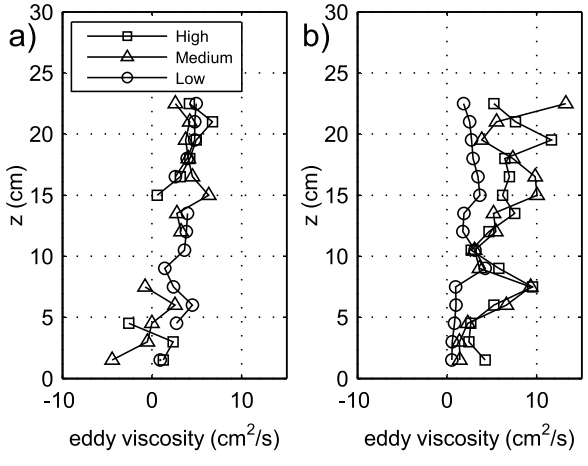

Figure 11. Eddy viscosity within the patch (a) and upstream of the patch (b), evaluated from (1) considering verticals at $x = 0$ and $x = 60$ cm.

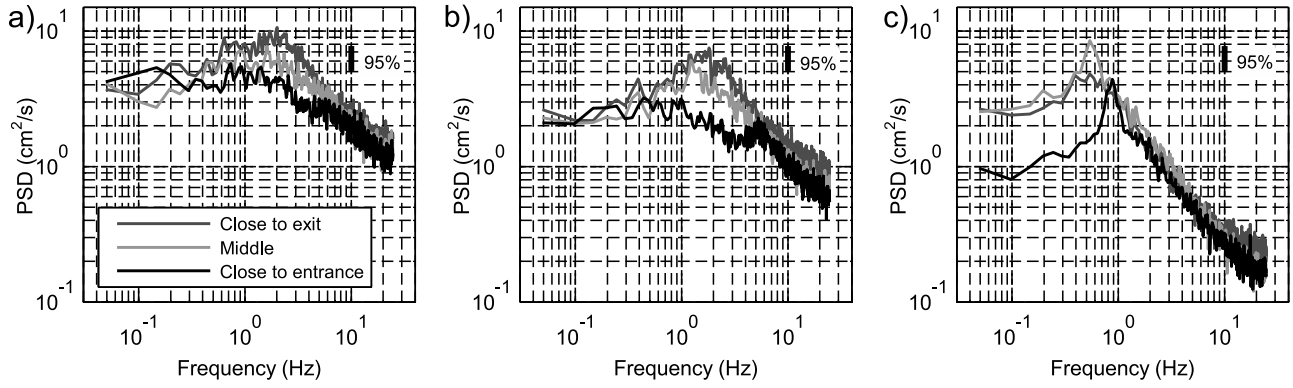

Figure 12. Power spectral densities of the transverse velocity within the patch for long-term measurements at high- (a), medium- (b), and low- (c) flow rates. The vertical bars indicate the 95% confidence intervals. The spectrum related to the velocity close to the entrance at low-flow rate (Figure 12c) shows smaller signal variance at low frequencies. This result is likely to be an effect of local conditions of flow turbulence during the experiment, which could affect single-point velocity measurements.

Nepf [2002]). We obtained $f_{KH} \sim 1.7$, 1.5, and 0.6 Hz, for high-, medium-, and low-flow rates, respectively.

3.2. Drag Forces

[27] This section describes the main findings related to the drag forces experienced by the individual plants within the vegetation patch.

3.2.1. Bulk Drag Parameters

[28] Data related to the three patch configurations (Figure 3) were used to estimate the bulk drag parameters for the entire patch. Statistical parameters of the drag force related to plants located at the same longitudinal but different transverse position were averaged, in order to obtain single-longitudinal profiles for each parameter. The mean value of the drag force D and noise-free standard deviation σ_d are plotted in Figure 13 for the high-flow rate scenario. The parameter σ_d was calculated by subtracting the noise variance (determined from noise floors in measured PSDs of drag force) from the total measured variance. The results reveal no significant spatial variation of the bulk drag parameters, except a weak reduction of the mean drag along the patch for the high- and medium-flow scenarios (at low-flow rate there is no defined pattern). The standard deviation follows a similar trend, although at the low-flow rate it slightly increases at the patch trailing edge.

[29] Direct measurements of drag forces allowed the calculation of the canopy drag length scale, which is a useful parameter for characterizing vegetated flows. It provides information on flow resistance within the obstruction [*Ghisalberti*, 2009] and it can be related to the vortex penetration length scale [*Nepf and Ghisalberti*, 2008]. This parameter was evaluated as $(C_d a)^{-1}$, where C_d is the plant drag coefficient and a is the frontal area per unit volume. The plant drag coefficient is often estimated from a momentum balance, considering uniform and steady state flow. In this study such an approach is not easily applicable because of the nonuniformity of the flow. Therefore, C_d was evaluated as an average of the drag coefficients related to the nine plants connected to the DFSs:

$$C_d = \overline{C_{d,i}} = \overline{\left(\frac{2D_i}{\rho A_i U_p^2}\right)}, \tag{2}$$

where D is mean drag force, A is the plant frontal area, U_p is mean velocity within the patch, and the subscript i relates to the ith plant ($i = 1, \ldots, 9$). A camera placed in a protective transparent box was used to take pictures of the plant frontal area, which was obtained as the area occupied by the plant in the picture. An estimate of a for each flow scenario was calculated as $N\overline{A_i}/(WL_p h_{\mathrm{veg}})$, where N is the number of plants ($N = 53$), $\overline{A_i}$ is the mean frontal area of the nine analyzed plants, W is the flume width, L_p is the patch length, and h_{veg} is the patch height. Using these data, we obtained drag length scales to be 79 cm (high flow), 82 cm (medium flow), and 48 cm (low flow).

[30] An estimate of the transition length L_T required for the flow encountering the patch to reach a new equilibrium

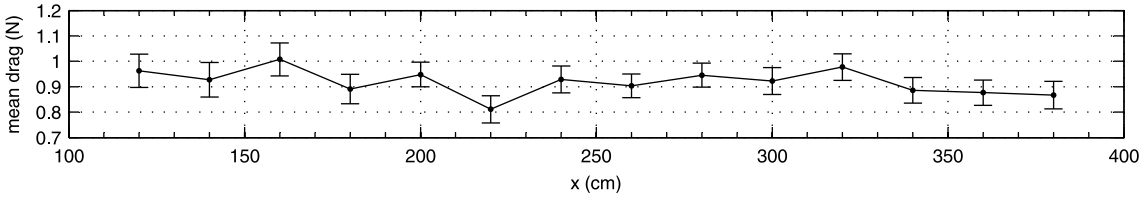

Figure 13. Longitudinal profile of mean drag force (high-flow rate scenario). Vertical bars relate to the standard deviation of fluctuating (in time) drag forces.

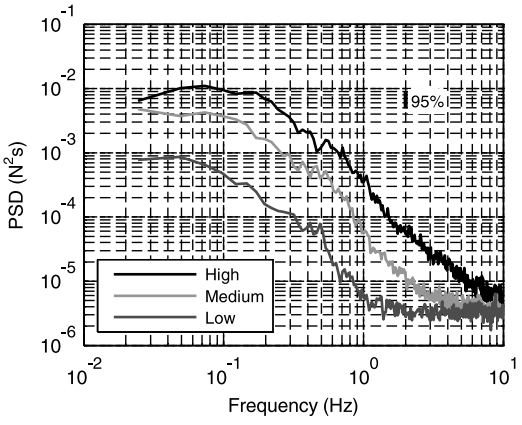

Figure 14. Power spectral densities of drag force fluctuations for high-, medium-, and low-flow rate scenarios (configuration 1, plant 1). The vertical bar indicates the 95% confidence interval.

state was also calculated, following *Ghisalberti and Nepf* [2009]:

$$L_T \approx 3\left(\frac{\overline{U}}{u_*}\right)(C_d a)^{-1}, \tag{3}$$

where u_* is the friction velocity determined using the patch-averaged Reynolds stresses. It is important to note that values of $\overline{U}$ and u_* for fully developed equilibrium flow condition should be used in this formula. In our study, however, this new equilibrium condition does not seem to be reached within the patch, as shown in Figures 4–7. Nevertheless, these estimates may provide qualitative information on flow adjustment within the patch. The transition lengths appeared to be $L_T \sim 32$ m (high-flow rate), 30 m (medium-flow rate), and 13 m (low-flow rate), which are much greater than the patch length (2.8 m), confirming the need for a much longer patch in order for the flow to reach a fully developed condition.

3.2.2. Spectral Analyses and Correlation Functions

[31] Examples of the power spectral density function for the drag fluctuations exerted on individual plants are shown in Figure 14. For all experiments, at low frequencies the spectra are flat and then, with an increase in frequency, the PSD decays, resembling a power function behavior. Similar behavior has been reported for drag spectra for several species of real aquatic plants (F. Siniscalchi and V. Nikora, personal communication). The spectral density is shown only up to 10 Hz since at higher frequencies the noise greatly affects the shape of the estimated spectra. For the low-flow rate scenario, the noise effect is already observable at 3–4 Hz, due to the reduced values of drag force fluctuations.

[32] Potential dependence of the drag forces on the fluctuating upstream velocity was analyzed by means of a cross-correlation function,

$$R_{u-d_i}(\tau) = \frac{\overline{u'(t)d_i'(t+\tau)}}{\sqrt{\sigma_u^2\sigma_{d_i}^2}}, \tag{4}$$

where τ is the time lag, u is the velocity measured upstream of the vegetation (see Figure 3), d_i is the drag force, and the subscript i relates to the force measured on the ith plant ($i = 1, \ldots, 9$). Cross-correlations between the upstream velocity and drag forces acting on the seven centerline plants (measured with DFS 3, 6, and 9 for the three patch configurations) were evaluated, and the peak values are shown in Figure 15a. For high- and medium-flow rates we note significant correlations between the two signals (at $p = 0.05$, the significance level ranged between 0.03 and 0.06 for both the high- and medium-flow rates; the large-lag standard errors for the cross-correlation estimates were evaluated according to *Box and Jenkins* [1970]). The correlation strength decreases with the separation distance. For the low-flow rate the correlation is much weaker and disappears 1 m downstream from the patch leading edge.

[33] An estimate of the velocity with which the drag signal responds to the upstream velocity signal can be obtained as the convection velocity:

$$C_v = \frac{L}{\tau_{\text{peak}}}, \tag{5}$$

where L is the distance between the upstream ADV sampling volume and the drag-measuring plants and τ_{peak} is the time lag related to the peak in the cross-correlation function (4). Results are presented in Figure 15b. Some points are missing because the corresponding cross-correlation function did not show a clearly identifiable peak (especially at the low-flow rate). For all cases, however, C_v appears to increase downstream toward the trailing edge. Moreover, its magnitude is comparable with the flow velocity above the patch, rather than inside it. Figure 16a presents examples of R_{u-d_i}, evaluated for plants 1, 3, and 9. The correlation between the upstream velocity and drag forces exerted on the plants in most experiments is denoted by a positive peak. In a few cases, however, negative peaks are found, especially in the high-flow rate scenario.

[34] Correlation analyses of drag time series were also performed. In most cases, a strong correlation was found among all drag-measuring plants, especially in the upstream part of the vegetation patch. Figure 16b shows the cross-correlation function $R_{d_i-d_j}$ evaluated using plants 1–7, 1–8, and 1–9 (configuration 1, high-flow rate). An interesting result that relates to the sign of the correlation peak should be noted. It appears that drag exerted on plants 1, 4,

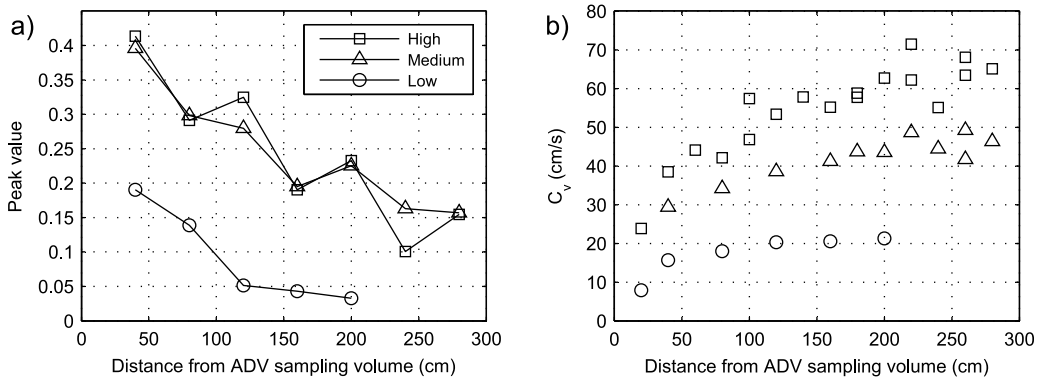

Figure 15. (a) Peak values of cross-correlation between upstream velocity and drag force exerted on the seven centerline plants, obtained using data from DFS 3, 6, and 9 for the three patch configurations; values related to plants located in the same position within the patch and obtained from different patch configurations were averaged. (b) Convection velocity evaluated from cross-correlations using equation (5), considering all nine plants; the presence of two data points at the same longitudinal distance indicates plants located at the same cross-section (e.g., plants 1–2, 4–5, and 7–8).

and 7 (which are closer to the left wall) in most cases is negatively correlated to the force exerted on the other analyzed plants, as well as to the upstream velocity. This is evident from the plots in Figure 16.

[35] Finally, cross-spectral analysis was used to investigate the dependence of the drag force fluctuations on the upstream velocity in the frequency domain. A useful parameter of the cross-spectra is the coherence function [e.g., *Bendat and Piersol*, 1993], defined as

$$\gamma^2_{u-d_i}(f) = \frac{|G_{u-d_i}(f)|^2}{G_u(f)G_{d_i}(f)}, \tag{6}$$

where G_{u-d_i} is the cross-spectrum between upstream velocity and drag force (for the ith plant) and G_u and G_{d_i} are the power spectral densities of the two time series. The coherence function is analogous to the squared cross-correlation function (4), but it reveals the frequency ranges which mainly contribute to the covariance of the signals. This parameter ranges from 0 to 1 and it was evaluated for all drag force time series at all flow rates. It is noted that, when correlation between upstream velocity and drag force exists, the related coherence function exhibits high values (in the range 0.2–0.6) at low frequencies, and then it rapidly approaches zero going toward higher frequencies. An example of coherence function is shown in Figure 17.

4. Discussion

[36] Mean velocities of the flow entering vegetated zones are reduced because of the additional drag forces exerted by the vegetation elements. The reduction in velocity is greatest in the upstream part of the patch, where a strong deceleration is found (Figure 5). This affects the TKE budget, since the term $-\overline{u'u'}(\partial\overline{u}/\partial x)$ of the total shear production $-\overline{u_i'u_j'}(\partial\overline{u_i}/\partial x_j)$ is positive and is likely to attain significant values appreciably enhancing the overall turbulence generation. As a result of this mechanism, a zone of increased turbulent energy appears at the patch entrance (Figure 6). A similar effect is found on the top of the patch, where the increased velocity gradient between flow regions above and within vegetation generates a shear layer, and associated increases in TKE (shear-generated turbulence). This region resembles the "vertical exchange zone" introduced by *Nepf and Vivoni* [2000] for aquatic canopies,

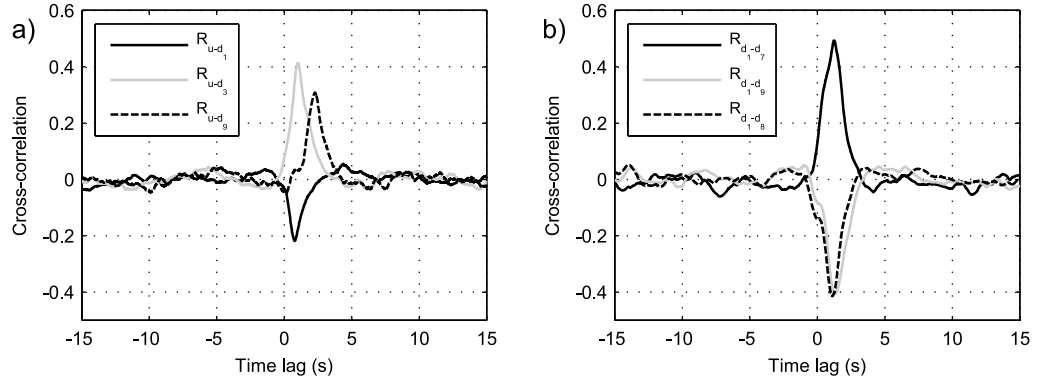

Figure 16. (a) Cross-correlations between upstream velocity and drag exerted on plants 1, 3, and 9 (high-flow rate scenario, configuration 1). (b) Cross-correlations between drag force acting on plants 1–7, 1–8, and 1–9 (high-flow rate scenario, configuration 1).

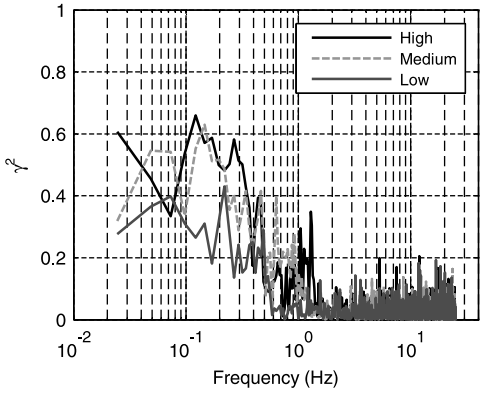

Figure 17. Coherence functions between upstream velocity and drag force exerted on plant 3 for all flow rate scenarios (configuration 1).

since the major contribution to the momentum balance is related to the vertical turbulent exchange. Below this region, in the lower canopy, *Nepf and Vivoni* [2000] defined a "longitudinal exchange zone," where vertical turbulent transport of momentum is negligible. In the present study, however, we often found $\langle -\overline{u'w'} \rangle < 0$ inside the patch (Figures 7 and 10b), with comparatively high-Reynolds stress magnitude. Negative Reynolds stresses indicate an upward vertical transport of momentum, being connected to negative velocity gradients $\partial \langle \overline{u} \rangle / \partial z < 0$, which are observable within the same flow regions (Figure 10a). As a consequence, the "spatially averaged" eddy viscosity coefficient is positive over the whole patch height. Locally, however, negative Reynolds stresses $-\overline{u'w'}$ are observed in some regions where positive velocity gradients $\partial \overline{u} / \partial z$ occur (Figures 8a–8f), indicating that there may be some localized regions within the patch where turbulent energy is transferred to the mean flow.

[37] The flow above the patch is characterized by $S_u < 0$ and $S_w > 0$, reflecting the tendency of relatively slow fluid parcels to move upward from the patch (an ejection-like motion). The same result was found by *Poggi et al.* [2004] above a uniform model canopy of rigid elements. On the contrary, downstream from the patch $S_u > 0$ and $S_w < 0$, and thus this wake flow region seems to be characterized by fast parcels moving toward the bed (a sweep-like motion).

[38] Interactions of flow with plants lead to additional mechanisms of energy conversion from the mean flow to turbulence, and this is revealed by the local increase of spectral energy shown in Figure 12. This turbulent energy production occurs in a range of frequencies, which is likely controlled by plant flexibility, arrangement, and morphology of the patch elements, as well as the velocity field. Similar modifications of velocity spectra were reported by *Nepf* [1999], *Finnigan* [2000], *Poggi and Katul* [2006], and *Naden et al.* [2006]. In the present study, close to the patch leading edge, the plant-wake-generated energy contribution appears in a restricted range of high frequencies, whereas further downstream inside the vegetation another mechanism of energy input emerges at lower frequencies as well. This effect is likely related to shear-scale energy production. The strong inflection point in the velocity profile at the top of the vegetation most likely generates coherent structures, which grow and develop along the patch length. At the leading edge, such eddies just start to develop, and therefore only the contribution of the plant-scale energy production is observable in the velocity PSD at high frequencies. Further downstream, the turbulent structures become more energetic and start penetrating into the patch. As a reflection of this, the measured spectra show an energy increase at lower frequencies, which in turn masks the wake-generated contribution (Figure 12).

[39] This physical picture is supported by the estimate of the length scales related to the low- and high-frequency spectral local maxima, $L_{\text{low}} = \overline{u_{\text{top}}}/f_{\text{low}}$ and $L_{\text{high}} = \overline{u_{\text{local}}}/f_{\text{high}}$, where $\overline{u_{\text{top}}}$ is the mean velocity at the top of the patch, $\overline{u_{\text{local}}}$ is the mean velocity at the measurement point, and f_{low} and f_{high} are the frequencies of the two PSD local peaks. We obtained $L_{\text{low}} \sim$36–42 cm and $L_{\text{high}} \sim$6–9 cm for all scenarios. The L_{low} is comparable with the external scale of the flow and is likely associated with the large shear-generated eddies flowing at the top of the vegetation. On the contrary, L_{high} is related to crown-wake turbulence. We cannot observe the stem-wake turbulence in our data because the ADV could not resolve scales smaller than the sampling volume size ($\sim$6–9 mm).

[40] Analyses of the drag force fluctuations also confirmed the physical picture presented so far. The significant correlation that we observe between upstream velocity and drag acting on the centerline plants along the entire length of the patch (for high- and medium-flow rates) suggests the presence of organized flow structures moving from the leading edge to the trailing edge, generating the drag fluctuations along the way. This is also verified by the high values of the coherence function at low frequencies, indicating that plants mainly respond to large-scale eddies as was also found by *Plew et al.* [2008], and by the strong correlation among drag time series in the measurement section. Furthermore, the magnitudes of the convection velocity appear to be consistent with the flow velocity at the top of the patch, and therefore drag fluctuations are likely related to turbulent structures flowing on the top of the plants. These structures appear to accelerate along the patch, and this might be due to the decreasing water level (Figure 4).

[41] Plants closer to the left wall (1, 4, and 7) seem to respond with opposite sign of drag fluctuations compared to the other six plants (Figure 16). This result suggests that the coherent vortices forming within the shear layer are strongly three-dimensional and cannot be approximated as 2-D structures, as is often assumed as part of the mixing-layer analogy for channel beds fully covered by vegetation [e.g., *Nepf and Ghisalberti*, 2008]. In fact, Figure 12 shows that the transverse velocity component, together with the other two components, plays a major role in the production of the turbulent energy, although such a component was often omitted in previous studies.

[42] The results described can be integrated together into a conceptual model as shown in Figure 18. The approach flow is likely characterized by cellular secondary currents because of the small aspect ratio ($\sim$2) of our flow. On encountering the vegetation patch, most of the flow is diverted to the top of the patch and the approach cells are forced to interact and merge together, generating a bigger single cell. This cell might be controlled by Kelvin-Helmholtz instabilities, as suggested by our results in section 3.1.3, but this speculation

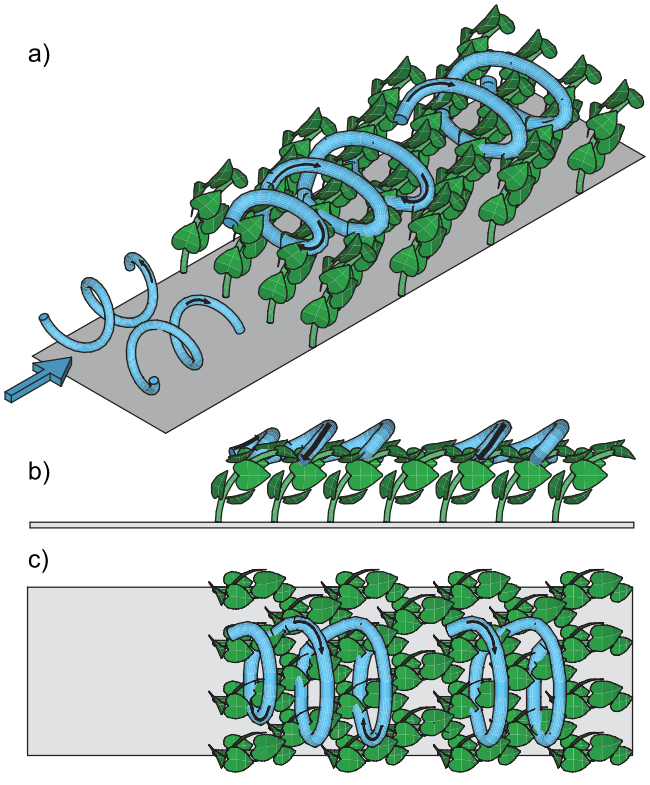

Figure 18. Conceptual picture of patch flow hydrodynamics: (a) parallel projection, (b) side view, and (c) plan view.

should be further investigated. Furthermore, because of the low relative submergence, the newly developed cell tends to expand in the spanwise direction, occupying a great part of the flume width. This hydrodynamic pattern leads to opposite fluctuations of the drag force related to plants located at opposite sides of the cell. This physical picture is in good agreement with the main findings of this study. However, it is only a first approximation and additional experiments would be required to elaborate on it further.

[43] *Nepf and Vivoni* [2000] described the transition between submerged and emergent regimes in aquatic canopies. Although in our experiments the depth ratio H/h_{veg} is close to 1 (especially for the low-flow rate), the results support the idea of considering the artificial patch as a submerged one, according to the *Nepf and Vivoni* [2000] classification. In fact, at high- and medium-flow rates, most of the flow encountering the vegetation is diverted to its top and a strong shear layer forms. This leads to the formation of 3-D coherent structures, which grow along the patch and enhance the vertical turbulent transport of momentum, as well as affecting the plant drag fluctuations. At the low-flow rate, part of the flow at the patch entrance is diverted to the near bed region as well, because of a particular reconfiguration of the vegetation elements, creating a preferential path near the flume bottom (Figure 5). However, as for the previous cases, organized structures appear to form at the top of the canopy where a shear layer is found.

[44] It is reasonable to speculate that three main hydrodynamic regions can be considered within vegetation patches. At the leading edge one can define an entrance region (1), where the interactions with the plants create significant longitudinal gradients of the velocity field, and additional turbulent energy production appears [e.g., *Bouma et al.*, 2007; *Neumeier*, 2007]. If the patch is long enough for the flow to reach a new equilibrium, a fully developed region (2) is formed [e.g., *Souliotis and Prinos*, 2011]. In this region, averaged flow and turbulence characteristics are statistically constant in the longitudinal direction. Finally, at the trailing edge, an exit region (3) can be identified, where the transition to the undisturbed condition occurs. A patch showing all three zones can be defined as a "hydrodynamically developed patch." In the present study, however, the flow appears not to reach an equilibrium state along the patch, thus a direct transition from zone (1) to (3) is observed, denoting a "hydrodynamically undeveloped patch." This is also indicated by the estimates of L_T in section 3.2.1. Further work is needed to clarify the subdivision and length of hydrodynamic regions in natural vegetation patches, which are likely to show hydrodynamically undeveloped patch conditions in both longitudinal and transverse directions. Other factors such as local flow conditions and plant density should also be investigated. For instance, *Ghisalberti and Nepf* [2009] explored the length of the entrance zone (1), arguing that this distance is governed not only by the fluid deceleration, but also by the shear layer growth. Patch density is expected to play an important role as well, since, the higher this parameter, the faster a new equilibrium is reached within the vegetated area, as shown by *Souliotis and Prinos* [2011].

5. Conclusions

[45] This paper examines the interactions between submerged vegetation and open-channel flows at the scale of a

plant patch. The experiments were conducted in a laboratory flume using a number of artificial flexible plants arranged in a staggered pattern, and synchronous data of flow velocities and drag forces were collected. Data processing included bulk statistics, spectral decomposition, and correlation analysis.

[46] It was shown that a strong shear layer formed on the top of the patch, which affected turbulent kinetic energy and Reynolds stresses, thus enhancing vertical turbulent transport of momentum. Moreover, a significant contribution to the production of TKE appeared to be related to the transverse component of velocity. Modifications of the longitudinal velocity profile and associated turbulent fluxes, connected to plant morphology and the degree of reconfiguration, were denoted by zones of negative Reynolds stresses within the patch. Interestingly, in the low-flow scenario, plants reconfigured in such a way that a preferential path also appeared near the bed, where velocities were found to be higher.

[47] The measurements of drag forces exerted on several plants within the patch provided further insights on flow-plant interactions. Drag force fluctuations were found to be significantly correlated with the velocity field fluctuations. This result, together with the additional mechanisms of energy production revealed by the velocity PSD, suggests the presence of large three-dimensional coherent structures at the top of the vegetation patch, which largely control the patch hydrodynamics.

[48] **Acknowledgments.** The authors would like to thank Benjamin Herzberg for his help in conducting the experiments, Thomas Schoneboom for his assistance with the DFS setup, and the Associate Editor and three anonymous reviewers for their detailed and helpful comments. The research was partly supported by the Leverhulme Trust, grant F/00152/Z "Biophysics of flow-plant interactions in aquatic systems," and Deutsche Forschungsgemeinschaft (AB 137/3).

References

Bendat, J. S., and A. G. Piersol (1993), *Engineering Applications of Correlation and Spectral Analysis*, 2nd ed., 458 pp., John Wiley, N. Y.

Bouma, T. J., L. A. van Duren, S. Temmerman, T. Claverie, A. Blanco-Garcia, T. Ysebaert, and P. M. J. Herman (2007), Spatial flow and sedimentation patterns within patches of epibenthic structures: Combining field, flume and modelling experiments, *Cont. Shelf Res.*, *27*, 1020–1045, doi:10.1016/j.csr.2005.12.019.

Box, G., and G. Jenkins (1970), *Time Series Analysis: Forecasting and Control*, 575 pp., Holden-Day, San Francisco, Calif.

Choi, S., and H. Kang (2004), Reynolds stress modeling of vegetated open-channel flows, *J. Hydraul. Res.*, *42*(1), 3–11, doi:10.1080/00221686.2004.9641178.

Ciraolo, G., G. B. Ferreri, and G. La Loggia (2006), Flow resistance of *Posidonia Oceanica* in shallow water, *J. Hydraul. Res.*, *44*(2), 189–202, doi:10.1080/00221686.2006.9521675.

Finnigan, J. (2000), Turbulence in plant canopies, *Annu. Rev. Fluid Mech.*, *32*, 519–571, doi:10.1146/annurev.fluid.32.1.519.

Folkard, A. M. (2005), Hydrodynamics of model *Posidonia Oceanica* patches in shallow water, *Limnol. Oceanogr.*, *50*(5), 1592–1600, doi:10.4319/lo.2005.50.5.1592.

Folkard, A. M. (2011a), Vegetated flows in their environmental context: A review, *Proc. Institution of Civil Engineers, Engineering and Computational Mechanics*, *164*(EM1), 3–24, doi:10.1680/eacm.8.00006.

Folkard, A. M. (2011b), Flow regimes in gaps within stands of flexible vegetation: Laboratory flume simulations, *Environ. Fluid Mech.*, *11*, 289–386, doi:10.1007/s10652-010-9197-5.

Garcia, C. M., P. R. Jackson, and M. H. Garcia (2005), Confidence intervals in the determination of turbulence parameters, *Exp. Fluid.*, *40*, 514–522, doi:10.1007/s00348-005-0091-8.

Ghisalberti, M. (2009), Obstructed shear flows: Similarities across systems and scales, *J. Fluid Mech.*, *641*, 51–61, doi:10.1017/S0022112009992175.

Ghisalberti, M., and H. Nepf (2002), Mixing layers and coherent structures in vegetated aquatic flows, *J. Geophys. Res.*, *107*(C2), 3011, doi:10.1029/2001JC000871.

Ghisalberti, M., and H. Nepf (2006), The structure of the shear layer in flows over rigid and flexible canopies, *Environ. Fluid Mech.*, *6*, 277–301, doi:10.1007/s10652-006-0002-4.

Ghisalberti, M., and H. Nepf (2009), Shallow flows over a permeable medium: The hydrodynamics of submerged aquatic canopies, *Transp. Porous Media*, *78*, 309–326, doi:10.1007/s11242-008-9305-x.

Goring, D. G., and V. I. Nikora (2002), Despiking acoustic doppler velocimeter data, *J. Hydraul. Eng.*, *128*(1), 117–126, doi:10.1061/(ASCE)0733-9429(2002)128:1(117).

Järvelä, J. (2005), Effect of submerged flexible vegetation on flow structure and resistance, *J. Hydrol.*, *307*, 233–241, doi:10.1016/j.jhydrol.2004.10.013.

Koch, E. W., J. D. Ackerman, J. Verduin, and M. van Keulen (2006), Fluid dynamics in seagrass ecology—from molecules to ecosystems, in *Seagrasses: Biology, Ecology and Conservation*, pp. 193–225, Springer, Dordrecht, Netherlands.

Lefebvre, A., C. E. L. Thompson, and C. L. Amos (2010), Influence of Zostera marina canopies on unidirectional flow, hydraulic roughness and sediment movement, *Cont. Shelf Res.*, *30*, 1783–1794, doi:10.1016/j.csr.2010.08.006.

Luhar, M., and H. M. Nepf (2011), Flow-induced reconfiguration of buoyant and flexible aquatic vegetation, *Limnol. Oceanogr.*, *56*(6), 2003–2017, doi:10.4319/lo.2011.56.6.2003.

Maltese, A., E. Cox, A. M. Folkard, G. Ciraolo, G. La Loggia, and G. Lombardo (2007), Laboratory measurements of flow and turbulence in discontinuous distributions of ligulate seagrass, *J. Hydraul. Eng.*, *133*(7), 750–760, doi:10.1061/(ASCE)0733-9429(2007)133:7(750).

Naden, P., P. Rameshwaran, O. Mountford, and C. Robertson (2006), The influence of macrophyte growth, typical of eutrophic conditions, on river flow velocities and turbulence production, *Hydrol. Processes*, *20*, 3915–3938, doi:10.1002/hyp.6165.

Nepf, H. (1999), Drag, turbulence and diffusion in flow through emergent vegetation, *Water Resour. Res.*, *35*(2), 479–489, doi:10.1029/1998WR900069.

Nepf, H., and M. Ghisalberti (2008), Flow and transport in channels with submerged vegetation, *Acta Geophysica*, *56*(3), 753–777, doi:10.2478/s11600-008-0017-y.

Nepf, H., and E. Vivoni (2000), Flow structure in depth-limited, vegetated flow, *J. Geophys. Res.*, *105*(C12), 28547–28557, doi:10.1029/2000JC900145.

Neumeier, U. (2007), Velocity and turbulence variations at the edge of saltmarshes, *Cont. Shelf Res.*, *27*, 1046–1059, doi:10.1016/j.csr.2005.07.009.

Nikora, V. (2010), Hydrodynamics of aquatic ecosystems: An interface between ecology, biomechanics and environmental fluid mechanics, *River Res. Appl.*, *26*, 367–384, doi:10.1002/rra.1291.

Plew, D. R., G. G. Cooper, and F. M. Callaghan (2008), Turbulence-induced forces in a freshwater macrophyte canopy, *Water Resour. Res.*, *44*, W02414, doi:10.1029/2007WR006064.

Poggi, D., and G. G. Katul (2006), Two-dimensional scalar spectra in the deeper layers of a dense and uniform model canopy, *Boundary Layer Meteorol.*, *121*, 267–281, doi:10.1007/s10546-006-9075-3.

Poggi, D., A. Porporato, L. Ridolfi, J. D. Albertson, and G. G. Katul (2004), The effect of vegetation density on canopy sub-layer turbulence, *Boundary Layer Meteorol.*, *111*, 565–587, doi:10.1023/B:BOUN.0000016576.05621.73.

Sand-Jensen, K. (2003), Drag and reconfiguration of freshwater macrophytes, *Freshwater Biol.*, *48*, 271–283, doi:10.1046/j.1365-2427.2003.00998.x.

Sand-Jensen, K., and O. Pedersen (1999), Velocity gradients and turbulence around macrophyte stands in streams, *Freshwater Biol.*, *42*, 315–328, doi:10.1046/j.1365-2427.1999.444495.x.

Schoneboom, T., and J. Aberle (2009), Influence of foliage on drag force of flexible vegetation, paper presented at the 33rd IAHR Congress, 9–14 August 2009, Vancouver, Canada.

Schoneboom, T., J. Aberle, C. A. M. E. Wilson, and A. Dittrich (2008), Drag force measurements of vegetation elements, paper presented at the 8th Internatl. Conf. on Hydro-Science and Engineering (ICHE 2008), 8–12 September 2008, Nagoya, Japan.

Schoneboom, T., J. Aberle, and A. Dittrich (2010), Hydraulic resistance of vegetated flows: Contribution of bed shear stress and vegetative drag to total hydraulic resistance, paper presented at the Internatl. Conf. on Fluvial Hydraulics (River Flow 2010), 8–10 September 2010, Braunschweig, Germany.

Souliotis, D., and P. Prinos (2011), Effect of a vegetation patch on turbulent channel flow, *J. Hydraul. Res.*, *49*(2), 157–167, doi:10.1080/00221686.2011.557258.

Sukhodolov, A. N., and T. A. Sukhodolova (2006), Evolution of mixing layers in turbulent flow over submersed vegetation: Field experiments and measurement study, paper presented at the Internatl. Conf. on Fluvial Hydraulics (River Flow 2006), 6–8 September 2006, Lisbon, Portugal.

Sukhodolov, A. N., and T. A. Sukhodolova (2010), Case study: Effect of submerged aquatic plants on turbulence structure in a lowland river, *J. Hydraul. Eng.*, *136*(7), 434–446, doi:10.1061/(ASCE)HY.1943-7900.0000195.

Zong, L., and H. Nepf (2010), Flow and deposition in and around a finite patch of vegetation, *Geomorphology*, *116*(3), 363–372, doi:10.1016/j.geomorph.2009.11.020.

J. Aberle, Leichtweiß-Institute for Hydraulic Engineering and Water Resources, Technische Universität Braunschweig, Beethovenstr. 51a, 38106 Braunschweig, Germany.

V. I. Nikora and F. Siniscalchi, School of Engineering, Fraser Noble Building, Elphinstone Road, University of Aberdeen, AB24 3UE Aberdeen, Scotland. (fabio.siniscalchi@abdn.ac.uk)